Nano Research

Open Access

Research Article

Zincophilic and hydrophobic bifunctional PFA-COOH-CNT artificial SEI film for highly stable Zn anode

Lingyao Kuang[1,§], Bohui Xu[2,§], Long Zhang[3], Zheshuai Lin[2], Xingxing Gu[1] ✉, Xiaolei Ren[1], and Yanglong Hou[3,4] ✉

[1] *Chongqing Key Laboratory of Catalysis and New Environmental Materials, College of Environment and Resources, Chongqing 400067, China*
[2] *Functional Crystals Lab, Technical Institute of Physics and Chemistry, Chinese Academy of Sciences, Beijing 100190, China*
[3] *School of Materials, Shenzhen Campus of Sun Yat-Sen University, Shenzhen 518107, China*
[4] *Beijing Key Laboratory for Magnetoelectric Materials and Devices (BKL-MMD), School of Materials Science and Engineering, Peking University, Beijing 100871, China*
§ *Lingyao Kuang and Bohui Xu contributed equally to this work.*

Cite this article: *Nano Research*, **2025**, *18*, 94907156. https://doi.org/10.26599/NR.2025.94907156

ABSTRACT: Aqueous zinc-ion batteries (AZIBs) are regarded as one of the most promising rivals in the upcoming high-energy secondary battery market because of their safety and non-toxicity. However, the zinc dendrites growth and hydrogen evolution corrosion of the Zn anode have seriously restricted the application of AZIBs. Herein, to overcome these constraints, a three-dimensional (3D) porous PFA-COOH-CNT artificial solid electrolyte interface (SEI) film with high hydrophobic and zincophilic properties was constructed on Zn anode surface by *in-situ* polymerization of furfuryl alcohol (FA) and carboxyl carbon nanotubes (COOH-CNT). A series of *in-situ*, *ex-situ* characterizations as well as the density functional theory (DFT) calculations reveal that the formed PFA-COOH-CNT SEI film with an abundant oxygen-containing group can provide abundant zincophilic sites and induce homogeneous deposition of Zn^{2+}, as well as the hydrophobic alkyl and carbon skeleton in PFA-COOH-CNT SEI film can isolate the direct contact of H_2O with Zn anode, and inhibit the occurrence of hydrogen evolution reaction (HER). Accordingly, the Zn anode with PFA-COOH-CNT layer can attain an ultra-long cycle life of 2200 h at 1 mA·cm^{-2}, 1 mAh·cm^{-2}. Simultaneously, the assembled PFA-COOH-CNT@Zn||V_2O_5 full cell can also achieve a high reversible capacity of up to 150.2 mAh·g^{-1} at 1 A·g^{-1} after 400 cycles, with a high average coulombic efficiency (CE) of 98.8 %. The designed PFA-COOH-CNT artificial SEI film provides a broad prospect for highly stable zinc anode, and can also be extended to other energy storage systems based on metal anodes.

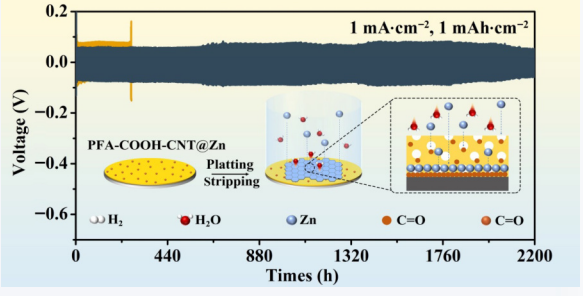

KEYWORDS: Zn anode, PFA-COOH-CNT solid electrolyte interface (SEI) film, zincophilic, hydrophobic

1 Introduction

Given the rapid growth of electric vehicles, portable electronic products and power grids, increased demands have been made on energy storage, and energy storage devices with high safety and stability have become a research hotspot [1]. As the requirements of energy storage become more and more stringent, energy storage devices are becoming more and more diverse [2]. Among the many options, aqueous zinc ion batteries (AZIBs) with high safety and stable charge–discharge are widely considered to be one of the most promising candidates [3]. As an important part of AZIBs, the Zn anode demonstrates the benefits of high natural abundance [4], high theoretical specific capacity (820 mAh·g^{-1}) and low redox potential (−0.762 V compared with standard hydrogen electrode) [5, 6]. However, zinc anodes are prone to Zn dendrite growth, hydrogen evolution reaction (HER), surface corrosion and other problems during the cycle, resulting in weak reversibility, low coulomb efficiency (CE), and low capacity attenuation, which hinder AZIBs further commercial application [7, 8].

To overcome the above problems, many strategies have been proposed to protect Zn anodes, including the three-dimensional (3D) Zn anode [9, 10], optimizing the electrolytes [11, 12], modifying the separators [13, 14], and constructing a surface protective layer [15, 16], etc. Among these strategies, the

Received: October 17, 2024; **Revised:** November 16, 2024
Accepted: November 25, 2024

✉Address correspondence to Xingxing Gu, x.gu@ctbu.edu.cn; Yanglong Hou, hou@pku.edu.cn

introduction of artificial solid electrolyte interface (SEI) film as a surface protective layer, is generally considered to be a favorable strategy for regulating the uniform deposition of Zn^{2+} and inhibiting the HER of Zn anode. In a variety of SEI films, some hydrophobic SEI films demonstrated the ability to repel water in aqueous electrolytes, but can not effectively adjust the Zn^{2+} uniform deposition [17, 18]; some zincophilic SEI films provide large amounts of zincophilic active site and a uniform flux of Zn^{2+} for realizing uniform deposition, but could not significantly prevent the H_2O molecule to corrode the Zn anode surface [18]. Therefore, it is crucial to construct a reasonable SEI film that demonstrates zincophilic and hydrophobic bi-properties to strike a balance between inducing uniform Zn^{2+} deposition and inhibiting HER and finally avoiding Zn dendrites growth.

Carbon materials, commonly with high conductivity, high specific surface area, excellent mechanical strength and hydrophobic properties [19, 20], have been widely reported as artificial SEI films to protect Zn anodes, mainly by forming a hydrophobic interface on the zinc foil surface, thereby reducing HER [21, 22]. Nevertheless, the zincophobic properties of these materials may hinder the transfer of Zn^{2+}, thus affecting the uniform deposition of Zn^{2+} [23]. While the organic SEI films containing polar functional groups can provide abundant zincophilic sites, which have the potential to induce uniform zinc deposition. However, organic SEI films usually have high interfacial resistance, resulting in low zinc ion conductivity and high polarizability [2, 24], which will greatly affect the electrochemical performance of zinc anodes at high current densities [17, 25]. Therefore, it is an effective solution to construct an artificial SEI film with hydrophobic surface, high zincophilic and high conductivity.

Therefore, in this work, we cleverly combine a kind of carbon material (carboxyl carbon nanotubes, COOH-CNT) with polar organic molecules (furfuryl alcohol, FA) to experience an *in-situ* reaction on the surface of zinc foil, as shown in Fig. 1(a), to form an artificial SEI film (PFA-COOH-CNT) that is both zincophilic and hydrophobic to stabilize the Zn anode. While plating or stripping, without the PFA-COOH-CNT SEI film, the Zn^{2+} ions deposition is not uniform and the naked Zn anode occurs serious HER, accompanying Zn dendrite growth, as illustrated in Fig. 1(b). While with the PFA-COOH-CNT SEI film on Zn anode, during plating/stripping process, the Zn^{2+} ions deposition is uniform as well as the side reactions and Zn dendrite growth are effectively inhibited. Accordingly, the assembled PFA-COOH-CNT@Zn||Zn symmetric battery cycling stability can reach 2200 h at 1 $mA{\cdot}cm^{-2}$, 1 $mAh{\cdot}cm^{-2}$, much longer than Zn||Zn symmetric battery (418 h). Meanwhile, the assembled PFA-COOH-CNT@Zn||V_2O_5 full cell also illustrates outstanding electrochemical performances, with the reversible capacity reaching 150.2 $mAh{\cdot}g^{-1}$ at 1 $A{\cdot}g^{-1}$ after 400 cycles. And a capacity decay is only 0.059% per cycle. Moreover, the CE of the full cells is also enhanced to 98.8%. Such advanced performances could give credit to the unique advantages of PFA-COOH-CNT SEI film: (i) the abundant polar oxygen-containing

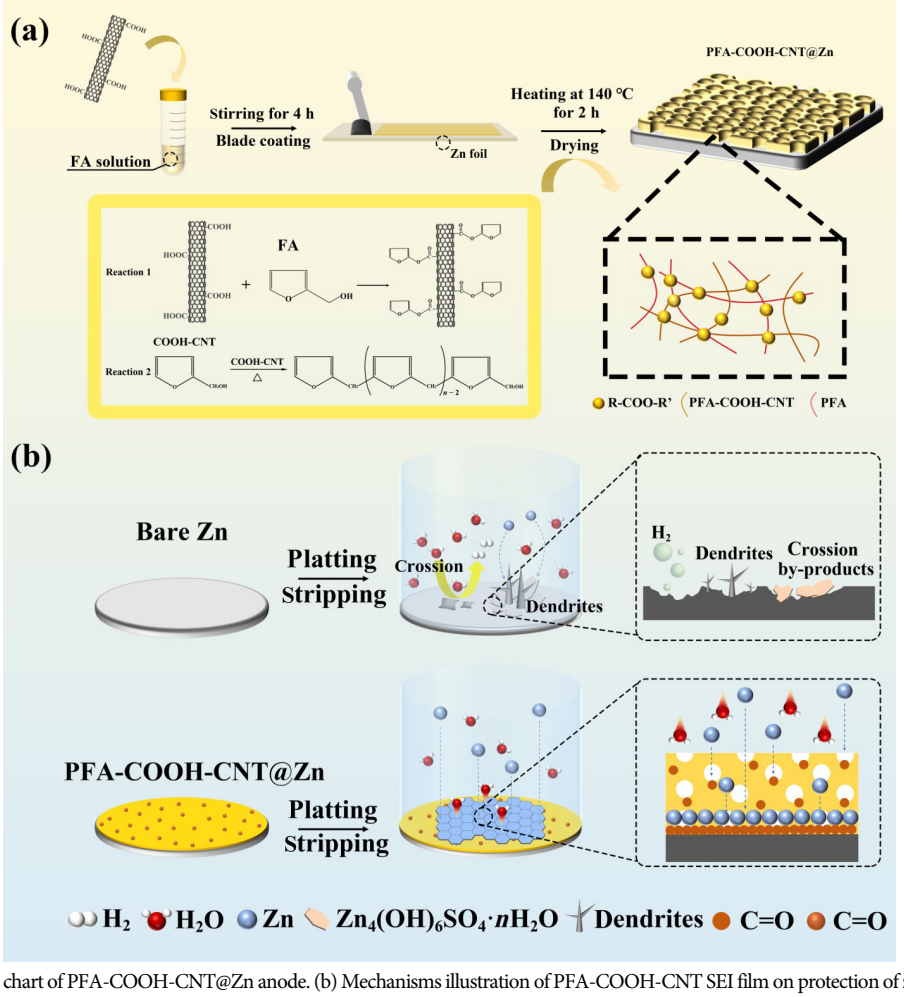

Figure 1 (a) Synthesis flow chart of PFA-COOH-CNT@Zn anode. (b) Mechanisms illustration of PFA-COOH-CNT SEI film on protection of zinc anode.

functional groups (C–O, C=O) in the SEI skeleton improve the zincophobic property and induce uniform deposition of Zn^{2+} ions; (ii) hydrophobic alkyl and carbon skeleton in SEI film physically isolate the active water and thus restrain the HER; (iii) a 3D porous structure inside the SEI film provides uniform ion flux, enhances the transport kinetics of Zn^{2+}, and inhibits the growth of zinc dendrites; and (iv) the ultra-high electrical conductivity of COOH-CNT improves the insulation of PFA and accelerates the transport efficiency of Zn^{2+} ions.

2 Experimental

2.1 Materials preparation

Preparation of PFA-COOH-CNT@Zn anode: 1.6 g of FA (99.7%, Aladdin) and 50 mg COOH-CNT (≥ 99.9%, Aladdin) were mixed homogenously at room temperature and then coated the slurry on Zn foil (99.9%, Saber Electrochemical Materials Co. 0.05 mm, 10 cm × 4 cm). Next, the coated Zn foil was put into the oven, 140 °C reaction for 2 h, and finally dried to obtain the PFA-COOH-CNT@Zn anode.

Preparation of PFA-CNT@Zn anode: 1.6 g of FA (99.7%, Aladdin) and 50 mg CNT (≥ 98%, Aladdin) were mixed homogenously at room temperature and then coated the slurry on Zn foil (99.9%, Saber Electrochemical Materials Co. 0.05 mm, 10 cm × 4 cm). Next, the coated Zn foil was put into the oven, 140 °C reacting for 2 h, and finally dried to obtain the PFA-CNT@Zn anode.

Preparation of PVDF-COOH-CNT@Zn anode: 1.6 mg of PVDF (AR, Saber Electrochemical Materials Co.) and 50 mg COOH-CNT (≥ 99.9%, Aladdin) were mixed homogenously at room temperature and then coated the slurry on Zn foil (99.9%, Saber Electrochemical Materials Co. 0.05 mm, 10 cm × 4 cm). Next, the coated Zn foil was put into the oven, heating at 140 °C for 2 h, to obtain the PVDF-COOH-CNT@Zn anode.

Preparation of PFA@Zn anode: 1.6 g of FA (99.7%, Aladdin) and 50 mg oxalic acid (OA, 99.7%, Aladdin) were mixed homogenously at room temperature and then coated the slurry on Zn foil (99.9%, Saber Electrochemical Materials Co. 0.05 mm, 10 cm × 4cm). Next, the coated Zn foil was put into the oven, 140 °C reaction for 2 h, and finally dried to obtain the PFA@Zn anode.

Synthesis of preconditioned V_2O_5 cathode: 1 g of commercial V_2O_5 (99.9%, Aladdin) powder was mixed with NaCl solution (≥ 99.5%, Aladdin, 15 mL, 2 mol·L^{-1}) at 25 °C and then stirred intensively to get a brown suspension. The brown suspension was centrifuged and repeatedly washed the product with distilled water and ethanol, and finally dried to get the V_2O_5.

Preparation of V_2O_5 cathodes: V_2O_5, conductive carbon black (AR, Saber Electrochemical Materials Co.), and PVDF were mixed with a mass ratio of 7:2:1. Then the mixture was stirred at room temperature (25 °C) for enough time and subsequently coated the homogenous slurry on stainless steel foil (99.9%, Saber Electrochemical Materials Co. 0.05 mm, R = 1.6 cm), 60 °C drying for 12 h to get the electrode. The loading mass of V_2O_5 cathode was around 1.5 mg·cm^{-2}.

2.2 Characterizations

A Bruker-d8 ADVANCE X-ray diffractometer was used to test the X-ray diffraction (XRD) spectroscopy. The morphologies of the materials were conducted on JSM-7001F (Nippon Electronics Co., LTD.) The materials composition and groups were characterized by Fourier infrared spectroscopy (FT-IR, Bruker VERTEX 80) and X-ray photoelectron spectroscopy (XPS, IRTracer 100, Shimadzu, Japan). The contact angle was tested by MY-SPCAX3.

2.3 *In-situ* electrochemical characterizations

In-situ digital holographic measurements (IDHM) were performed synchronously in a two-electrode system assembled in a transparent optical cell. The optical cell is a cube with a side length of 5 cm. CHI 660E station (Shanghai Chenhua) was used to conduct test for IDHM. During the test, electroplating was conducted for 1.5 min at 4.0 mA·cm^{-2}, and two zinc foil was used as the working electrode and the opposite electrode. 60 mL 2 M $ZnSO_4$ (ZSO) electrolyte was added for testing. Before each test, the working Zn anode was ground with various wet sandpapers with different particle sizes.

In situ differential electrochemical mass spectra (DEMS) was conducted on QAS100 to determine the hydrogen evolution intensity. During test, two zinc foil was used as the working electrode and the opposite electrode, and 2 M ZSO solution was used as the electrolyte.

2.4 *Ex-situ* electrochemical test

Assembly of the battery: Pure Zn anode and various modified Zn anodes were employed in Zn||Zn symmetrical batteries, Zn||Cu, Zn||Ti asymmetric batteries and Zn||V_2O_5 full batteries. The Cu foil (99.9%, Saber Electrochemical Materials Co., 0.05 mm, R = 1.6 cm) and Ti foil (99.9%, Aladdin, 0.1 mm, R = 1.6 cm) were used in Zn||Cu and Zn||Ti asymmetric batteries, respectively. In addition, the prepared V_2O_5 cathode was employed to assemble in Zn||V_2O_5 full batteries. The 2 mol·L^{-1} $ZnSO_4$ solution was used as the electrolyte and Whatman glass fiber (~ 260 μm, GF/D grade) was used as the separator.

The Zn||Zn symmetric batteries, Zn||Cu and Zn||Ti half cells and Zn||V_2O_5 full batteries were assembled in a glove box using the CR2032 battery model. Galvanostatic tests, nucleation overpotential and Coulombic efficiency tests were performed on Land battery test system (LAND-CT2001A, Wuhan). The cyclic voltammetry (CV), electrochemical impedance spectroscopy (EIS), Tafel curves, chronoamperometric method (CA), and linear voltammetry scanning (LSV) were tested at CHI 660E station too.

2.5 Calculations

Density functional theory (DFT) calculations for binding energy were carried out using the density functional plane-wave pseudopotential approach on the CASTEP program [26]. For geometric optimization, the Broyden Fletcher Goldfarb Shanno (BFGS) minimization technique was used [27]. A set of requirements (1×10^{-5} eV·$atom^{-1}$, 0.03 eV·$é^{-1}$, 0.02 GPa, and 0.001 Å) was established for the convergence of energy, maximum force, maximum stress, and maximum displacement. The exchange correlation energy was chosen to be described by the Perdew–Burke–Ernzerhof (PBE) functionals in the generalized gradient approximation [28]. The DFT-D3 approach was utilized to accurately predict the adsorption strength [29]. To construct the Zn (002) slab model, a 15 Å vacuum layer and a (4 × 4) unit cell were built [30]. The X@Zn (002) (X = PFA, CNT, COOH-CNT, PFA-COOH-CNT and PVDF) surface was modeled by adsorbing several repeating units of polymer X on the pristine Zn (002) surface. The adsorption energy (ΔE) was calculated according to the equation

$$\Delta E = E_{total} - E_{X@Zn} - E_{H_2O/Zn}$$

where E_{total} is the total energy of the optimized surface system with adsorbate H_2O/Zn on. $E_{X@Zn}$ and $E_{H2O/Zn}$ represent the energy of the Zn (002) with SEI film X and the adsorbents H_2O/Zn in the vacuum slab, respectively.

3 Results and discussion

The polymerization of FA and COOH-CNT on zinc foil was confirmed through a series of characterization tests. As depicted in Fig. 2(a), original COOH-CNT exhibits relatively sharp diffraction peaks at 2θ of 26° and 43°, belonging to the graphitization peak of carbon, in accord with the previous literature reports [31, 32]. The PFA formed by polymerization of FA will display a wide diffraction peak at around two theta of 23°, corresponding to the characteristic diffraction peak of phenolic resin [33]. While it can be seen the PFA-COOH-CNT samples show a wide peak at around 20°, moving towards a small angle compared to the original COOH-CNT and FA samples. In addition, the sharp peak at 2θ of 43° has almost disappeared. These changes in XRD spectra are most likely due to happen esterification reaction between FA and COOH-CNT. Then the occurrence of self-polymerization for FA and esterification reaction between FA and COOH-CNT was investigated using FT-IR. As depicted in Fig. 2(b), COOH-CNT sample illustrates O–H stretching vibration absorption peak (3430 cm^{-1}), C=C stretching vibration (1600 cm^{-1}), C=O stretching vibration (1720 cm^{-1}), and C-O stretching vibration (1170 cm^{-1}) [34]. While FA exhibits a characteristic absorption peak at 3338, 2927 and 2872 cm^{-1}, ascribed to the stretching vibration of O–H, C–H and –CH_2 stretching vibrations [35]. The previous studies revealed that under acidic conditions, the FA would happen self-polymerizion to form PFA, corresponding the O–H characteristic absorption peak at 3338 cm^{-1} significantly diminished and the furan ring characteristic absorption peak on FA at 1504 cm^{-1} also weakened [35, 36]. The pH test in Fig. S1 in the Electronic Supplementary Material (ESM) shows the similar acidic environment of FA and COOH-CNT and the FA and OA mixed solution, also indicating the high probability of reaction between FA and COOH-CNT. As expected, from the FT-IR spectra of PFA and PFA-COOH CNT, we can clearly observe the disappearance of the O–H characteristic absorption peak, as well as the more weakened furan ring characteristic absorption peak, indicating the successful self-polymerization of FA during the form of PFA and PFA-COOH-CNT SEI film. Moreover, compared to the single adsorption peak (1720 cm^{-1}) of C=O bond in COOH-CNT, it should be noted that the adsorption peak of C=O bond in PFA-COOH-CNT has split into two positions (1762 and 1707 cm^{-1}), which may be because a part of –COOH groups reacts with –OH groups to happen esterification reaction. The shift of adsorption peak of C–O bond (1063 cm^{-1}) in PFA-COOH-CNT in comparison with that in COOH-CNT could also prove the possible esterification reaction. In addition to the FT-IR characterization, the XPS characterization was also performed to explore the self-polymerization of FA and the esterification reaction between FA and COOH-CNT. As revealed in high-resolution C 1s XPS spectrum of Fig. 2(c), the peak of O–C=O bond belongs to carboxyl in COOH-CNT and is located at 291.5 eV, while the peak of O–C=O bond in PFA-COOH-CNT shifts to low binding energy, which is because there are not only carboxyl groups but also ester groups [37, 38]. The same trend for O–C=O bond can also be observed in the high-resolution map of O 1s as shown in Fig. 2(d). Moreover, from O 1s spectrum, it can be observed the strong peak of C–OH bond at 530.5 eV in COOH-CNT, but this peak almost disappears in PFA-COOH-CNT sample, which is also because of the esterification reaction [39]. From the C 1s spectrum, it can also be clearly observed that the peak of C–O–C in FA locates at 286.9 eV, while it shifts to a low binding energy of 286.0 eV in PFA and PFA-COOH-CNT, indicating the self-polymerization of FA happened. And there are also shifts for C–O–C bond in O 1s spectrum, again indicating the self-polymerization of FA. The above characterization fully proves that FA and COOH-CNT can undergo *in-situ* polymerization on the surface of zinc foil to form an SEI film with zincophilic oxygen-containing groups and hydrophobic alkyl groups, which will control zinc ion homogeneous deposition and prevent dendritic development.

Finally, the morphologies of these SEI films were investigated by the SEM at different size. As can be seen in Fig. 2(e), the PFA SEI film on the Zn anode is very dense, which is not beneficial for

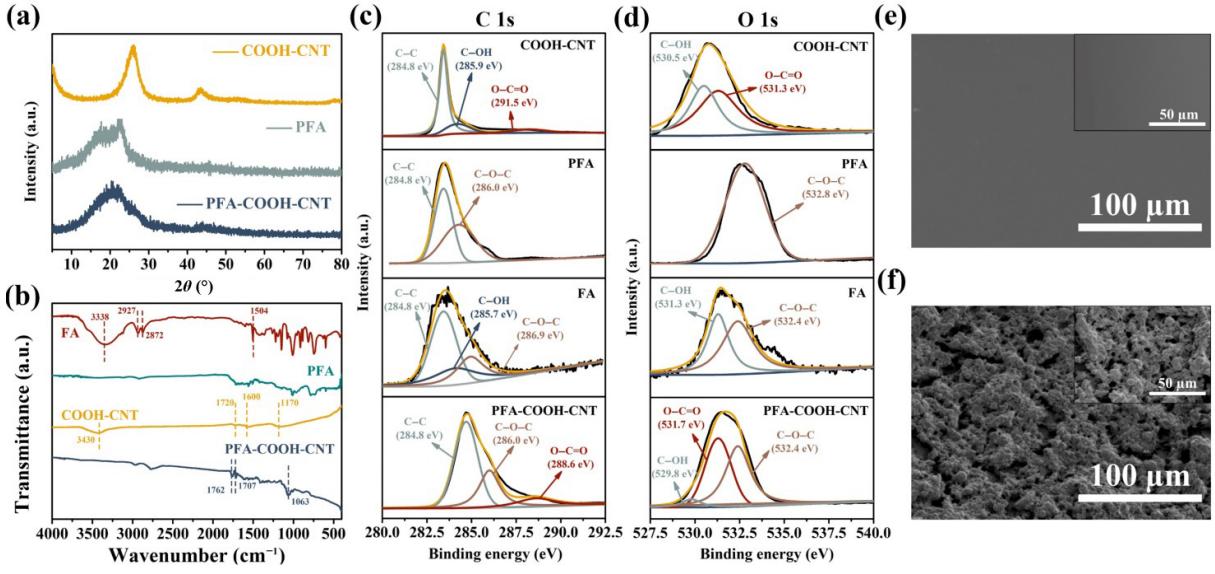

Figure 2 Synthesis and material characterization of PFA-COOH-CNT SEI film. (a) XRD spectra of COOH-CNT, PFA, and PFA-COOH-CNT, (b) FT-IR spectra of FA, PFA, COOH-CNT, and PFA-COOH-CNT, (c) high-resolution XPS of C 1s, (d) high-resolution XPS of O 1s, SEM images of (e) PFA@Zn (top view) and (f) PFA-COOH-CNT@Zn (top view).

electrolyte infiltration and the ion transport. Whether it's 100 or 50 μm in size, the surfaces of PFA-COOH-CNT (Fig. 2(f)), PFA-CNT (Fig. S2(a) in the ESM) and PVDF-COOH-CNT (Fig. S2(b) in the ESM) films on the Zn anode are not dense and illustrate loose and porous structure. And even from the side view observation, it still can be observed the abundant pore structures and cracks (Fig. S2(c) in the ESM), which suggest the PFA-COOH-CNT film with the 3D porous structure in the whole framework and is very conducive to electrolyte infiltration and ion transport, so as to achieve good electrochemical performance of zinc anode. Meanwhile, the thickness of different SEI films is compared in Fig. S2(c)–S2(f) in the ESM. The thickness of PFA-COOH-CNT film is moderate (25 μm), which not only satisfies the rapid transport of zinc ions, but also prevents the contact between water molecules and zinc foil.

To evaluate the PFA-COOH-CNT films superiorities in stabilizing the Zn anode, the electrochemical performances of symmetrical Zn||Zn batteries were first investigated. Fig. 3(a) demonstrates the constant current charge and discharge curve for the pure Zn and coated Zn anode at the condition of 1 mA·cm^{-2}, 1 mAh·cm^{-2}. As can be seen, the symmetrical Zn||Zn batteries based on bare zinc anodes demonstrate unstable voltage and high voltage polarization with short circuits occurring in less than 300 cycles (263 h), possibly due to their susceptibility to corrosion without an SEI film, leading to byproduct formation and battery short-circuiting. In contrast, the Zn anodes with SEI films,whether they are PFA-CNT, PVDF-COOH-CNT, PFA, or PFA-COOH-CNT, demonstrate enhanced cycling stability (466 h for PFA@Zn, 708 h for PFA-CNT@Zn, 479 h for PVDF-COOH-CNT@Zn, and 2200 h for PFA-COOH-CNT@Zn). In addition to the PFA-COOH-CNT@Zn anode illustrating the longest stability, it also exhibits the most stable voltage and lowest voltage polarization. What's more, at

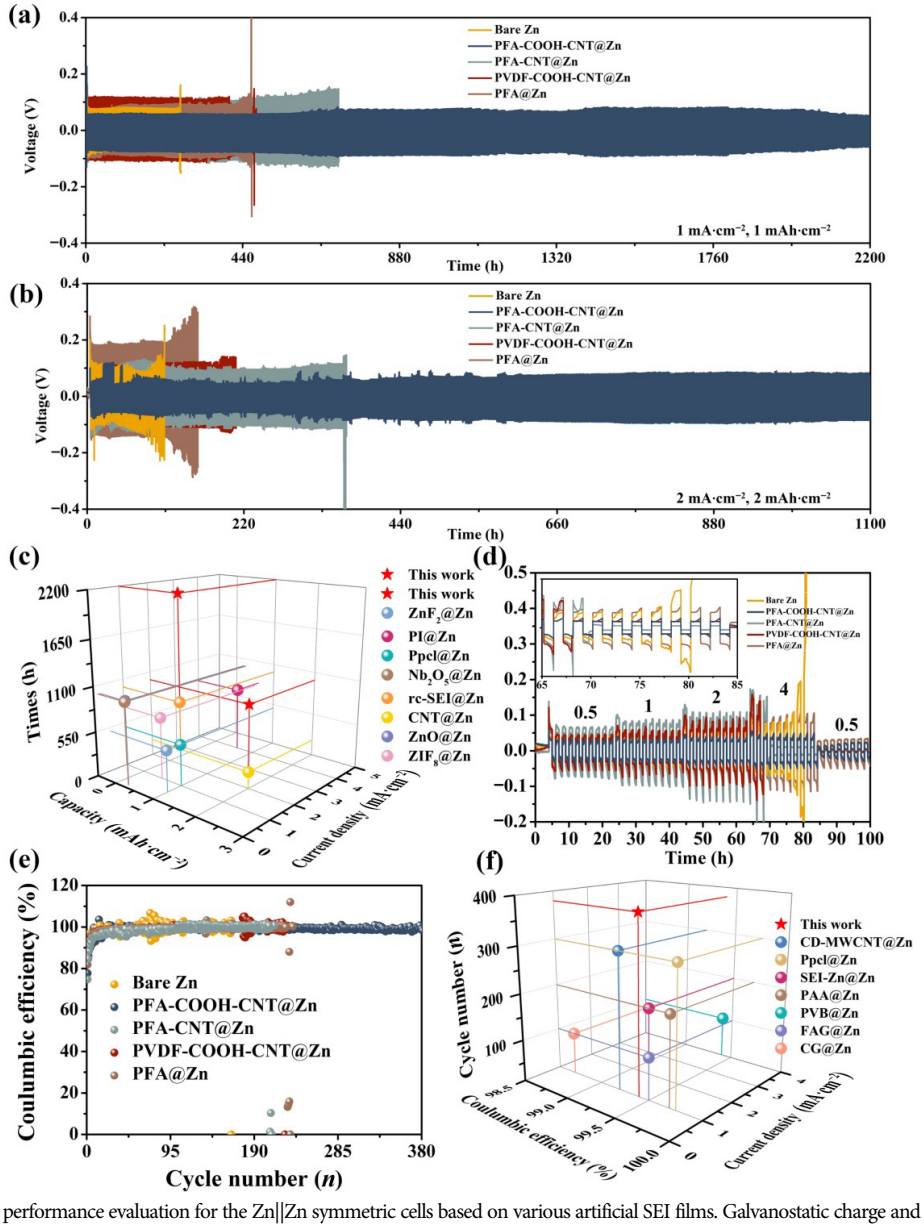

Figure 3 Electrochemical performance evaluation for the Zn||Zn symmetric cells based on various artificial SEI films. Galvanostatic charge and discharge curve of Zn||Zn cells at (a) 1 mA·cm^{-2}, 1 mAh·cm^{-2} and (b) 2 mA·cm^{-2}, 2 mAh·cm^{-2}. (c) Comparison of cycle life of PFA-COOH-CNT@Zn anode with previous works. (d) Cycle rate performance of Zn||Zn cells at 0.5, 1, 2, 4 and 0.5 mA·cm^{-2}, respectively. (e) Coulombic efficiency of Zn||Cu battery. (f) Comparison of CE of PFA-COOH-CNT@Zn anode with previous works.

a high discharge current of 2 mA·cm^{-2} and high capacity of 2 mAh·cm^{-2}, the symmetrical Zn||Zn batteries based on the coating Zn anodes also demonstrate better electrochemical performances compared to the bare Zn anode as shown in Fig. 3(b), particularly the PFA-COOH-CNT@Zn anode still shows the most stable cycle performance, up to 1100 h. More significantly, the PFA-COOH-CNT@Zn symmetric cell exhibits better voltage hysteresis and cycling life than the majority of Zn anodes modified with other SEI coatings (Fig. 3(c) and Table S1 in the ESM). In addition, the rate capabilities of PFA-COOH-CNT@Zn and other Zn anodes in symmetric cells at different current densities (0.5, 1, 2, and 4 mA·cm^{-2}) have also been evaluated (Fig. 3(d)). With the bare Zn and PFA@Zn anodes, the overpotential suddenly drops after about 70 h at a current density of 4 mA·cm^{-2}, which is considered to be a short circuit. While the PFA-COOH-CNT@Zn anode shows cycling stability after several cycles compared to PFA-CNT@Zn and PVDF-COOH-CNT@Zn anodes, a relatively constant voltage hysteresis has been observed even at 4 mA·cm^{-2}. Furthermore, the plating and stripping of Zn^{2+} on the surface of Zn anode during the CE tests reflect dendrite growth, which can further demonstrate the superiority of PFA-COOH-CNT SEI film in stabilizing zinc anode [40]. Therefore, the CE of the asymmetric Zn||Cu batteries based on naked Zn anode and coated Zn anode were then investigated. As depicted in Fig. 3(e), PFA-COOH-CNT@Zn anode maintains a high average CE of 99.2% over 380 long cycles. However, other coated Zn anodes as well as the bare Zn anode demonstrate large fluctuations in CE, and the average CEs are all lower than 90%. Finally, we compared the CE of the PFA-COOH-CNT@Zn anode with the previous reports Zn anodes with SEI films as shown in Fig. 3(f) and Tabel S2 in the ESM. As can be seen, the PFA-COOH-CNT@Zn anode demonstrates better cycling stability and CE than many previous studies.

To verify the mechanisms of PFA-COOH-CNT on stabilization of Zn anode, a variety of *in-situ* and *ex-situ* characterizations and theoretical calculations have been carried out. First, the adsorption energies of zinc atom on the surface of naked Zn anode and on the surface of zinc anode with different SEI films have been calculated by DFT. As can be seen in Fig. 4(a), the adsorption energy of Zn atom on the bare Zn surface is only −0.132 eV, while on the PVDF@Zn andCNT@Zn anode surface are −0.116 and −0.131 eV, respectively, indicating the PVDF and CNT won't increase zincophilic properties. However, the adsorption energies on PFA@Zn, COOH-CNT@Zn and PFA-COOH-CNT@Zn surfaces increase to −0.220, −0.255 and −0.278 eV, respectively, indicating the PFA and COOH-CNT could increase the zincophile property, particularly when combined with the PFA and COOH-CNT, the zincophilic property will be further improved. The zincophilic property of PFA-COOH-CNT could be attributed to numerous zincophilic sites provided by abundant oxygen-containing groups in PFA-COOH-CNT. Following the adsorption energies of H_2O molecules on Zn(002) surface and the surface of the zinc anode containing different SEI film components were calculated as well. As shown in Fig. 4(b), the adsorption energy of H_2O on Zn (002) surface is −0.473 eV, far higher than that on PVDF@Zn (−0.152 eV), PFA@Zn (−0.299 eV), CNT@Zn (−0.107 eV), COOH-CNT@Zn (−0.147 eV) and PFA-COOH-CNT@Zn (−0.207 eV) surfaces, indicating the hydrophobicity increase after introducing these SEI films on the Zn anode surface. Particularly the adsorption energy on CNT@Zn is the smallest, which is most likely due to the lack of highly electronegative functional groups, such as those containing oxygen and fluorine. These electronegative functional groups are conducive to forming hydrogen bonds with H_2O molecules and thus becoming hydrophilic. Therefore, the hydrophobicity of these SEI films should be attributed to the hydrophobic alkyl and carbon skeleton that are all present in PVDF, PFA, CNT, and COOH-CNT. The contact angle experiments also prove the hydrophobicity of these SEI films. As depicted in Fig. S(3) in the ESM, initially, the contact angle of ZSO solution on PFA-COOH-CNT@Zn surface is 78.8°, smaller than that of PFA-CNT@Zn (135.3°) and PVDF-COOH-CNT@Zn (121.1°), but higher than PFA@Zn (68.0°) and naked Zn (64.2°), which agrees with the calculation's findings. After 1 min of standing, the contact angles all decrease as shown in Fig. S4 in the ESM, but still maintain a similar trend as the initial state. According to the calculation and contact angle experiment results, the zincophilic and hydrophobic properties of PFA-COOH-CNT SEI film have been verified. Hydrophobicity of the SEI films can physically isolate water from contact with the zinc the zinc anode to inhibit the HER corrosion, however, excessive hydrophobicity may impede Zn^{2+} transmission [41]. Therefore, the PFA-COOH-CNT artificial SEI film with a moderate hydrophobicity and an excellent zincophilic property could most efficiently adjust the Zn^{2+} uniform deposition, prevent HER, and stabilize the negative zinc electrode.

Then the XRD and SEM characterizations were conducted to prove the PFA-COOH-CNT SEI film on significantly stabilize the Zn anode. As depicted in Fig. 4(c), in addition to PFA-COOH-CNT@Zn, different degree of by-products were observed on the surfaces of naked Zn and other coating Zn anodes after cycling 150 cycles, indicating the PFA-COOH-CNT SEI film was the most effective in inhibiting the formation of corrosion by-products. What's more, as illustrated in Fig. 4(d), the peak intensity ratio of Zn (002) to Zn (101), namely $I(002)/I(101)$, is the largest for PFA-COOH-CNT@Zn anode after cycling 150 cycles compared to other Zn anodes, suggesting more uniform deposition of Zn^{2+} and better inhibition of Zn dendrites during cycling [42]. Figures 4(e)–4(i) depicts the SEM images of different Zn anodes after 150 cycles. Corresponding to the XRD results, the surfaces of the naked Zn, PFA@Zn, PFA-CNT@Zn, PVDF-COOH-CNT@Zn anodes demonstrate a significant presence of sharp Zn dendrite growth and irregular by-products except PFA-COOH-CNT@Zn anode, also indicating that the ability of PFA-COOH-CNT SEI film on inhibiting of Zn dendrite growth and Zn anode corrosion surpasses other SEI films.

Except for these *ex-situ* material characterizations for exploring the mechanisms, the *in-situ* and *ex-situ* electrochemical characterizations also explored the mechanisms. First, the *in-situ* electrochemical characterization, IDHM was carried out to reveal the distributions of optical differences at the interface between Zn anode and electrolyte from the deposition time of 0 to 50 s. As depicted in Figs. 5(a) and 5(b), and Fig. S5 in the ESM, the top of the phase map represents the electrolyte, while the electrode is on the bottom. The black line indicates the electrode–electrolyte interface. A shift in the phase difference ($\Delta\Phi$) and ultimately a movement in the color difference can result from any variation in the ion concentration in the electrolyte. $\Delta\Phi > 0$ and $\Delta\Phi < 0$ represent the ion concentration increase and decrease, respectively. As can be seen in Fig. 5(a), with increasing time, the color gradually turns blue and obvious blue appears after only 10 s for the naked Zn anode surface. This phenomenon suggests a drop in ion concentration at the electrode interface as well as an

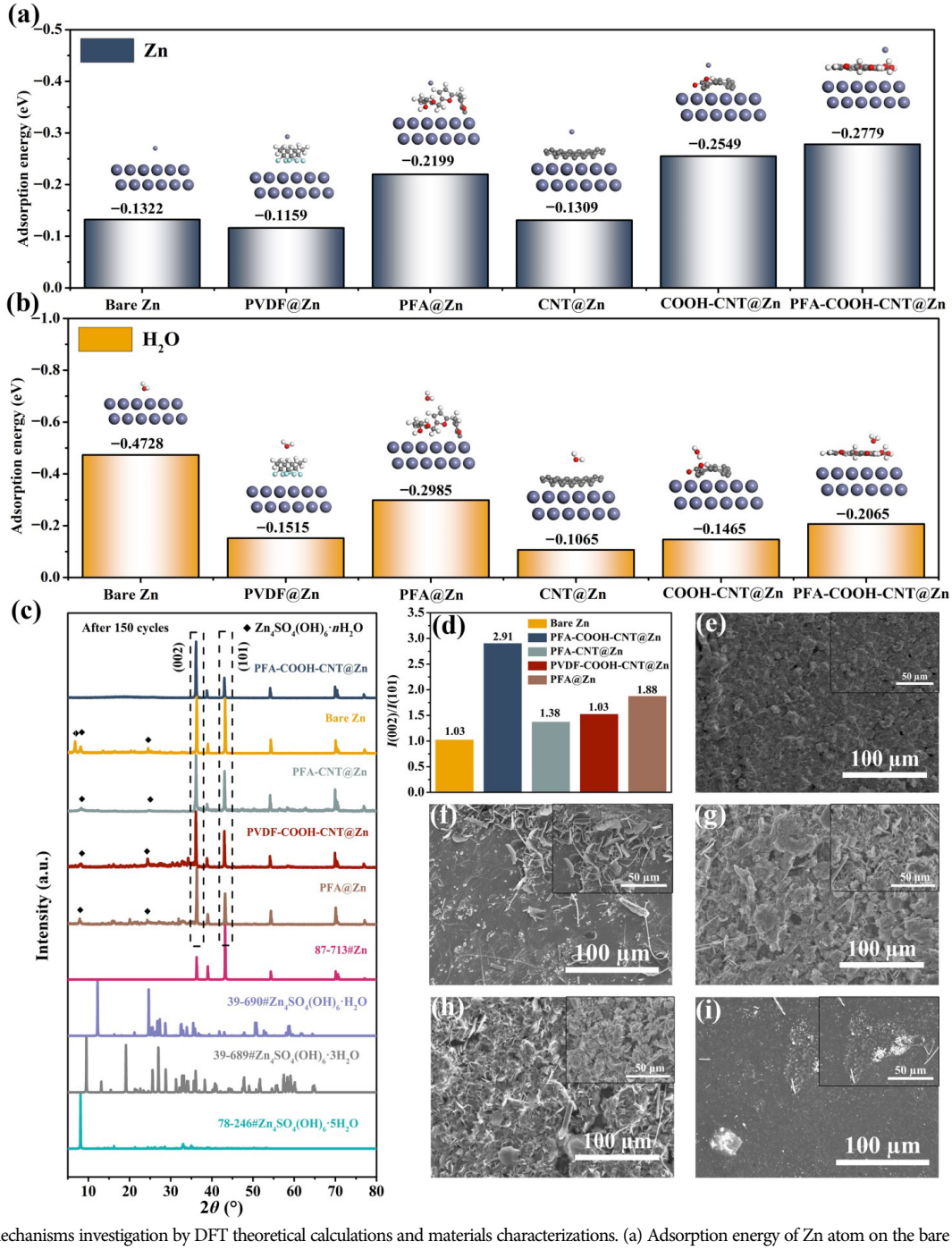

Figure 4 The mechanisms investigation by DFT theoretical calculations and materials characterizations. (a) Adsorption energy of Zn atom on the bare Zn anode surface and Zn anode surface with different SEI films. (b) Adsorption energy of H_2O molecule on the bare Zn anode surface and Zn anode surface with different SEI films. (c) XRD patterns of naked Zn anode and coating Zn anodes after 150 cycles at 1 mA·cm^{-2}. (d) The intensity comparison of $I(002)/I(101)$ for naked Zn anode and coating Zn anodes. Surface SEM images of (e) PFA-COOH-CNT@Zn, (f) bare Zn, (g) PFA-CNT@Zn, (h) PVDF-COOH-CNT@Zn, and (i) PFA@Zn.

inhomogeneous ion flux there. It is probably due to a large amount of Zn^{2+} consumption. What's more, the light blue area distributes unevenly in 50 s on PVDF-COOH-CNT@Zn (Fig. S5(a) in the ESM) and PFA@Zn (Fig. S5(b) in the ESM) anodes, suggesting incomplete zinc ion transport. For the PFA@Zn (Fig. S5(c) in the ESM) anode, obvious blue appears at 50 s, which also means that the uneven Zn deposition appears in PFA@Zn anodes. While only the PFA-COOH-CNT@Zn anode, with increasing the time, the color is always the same as the green in the first test, as shown in Fig. 5(b), which indicates that the "tip effect" is extremely weak, and the accumulation of electrons reduces as well as prevents dendritic growth on the anode. Therefore, the IDHM characterizations have confirmed that the zincophilic and hydrophobic bifunction of PFA-COOH-CNT could effectively induce uniform deposition sites for Zn^{2+}.

The CA curves for the different Zn-Ti cells also confirm the PFA-COOH-CNT SEI films could adjust the Zn^{2+} uniform deposition. As revealed in Fig. 5(c), during the galvanizing process, the current

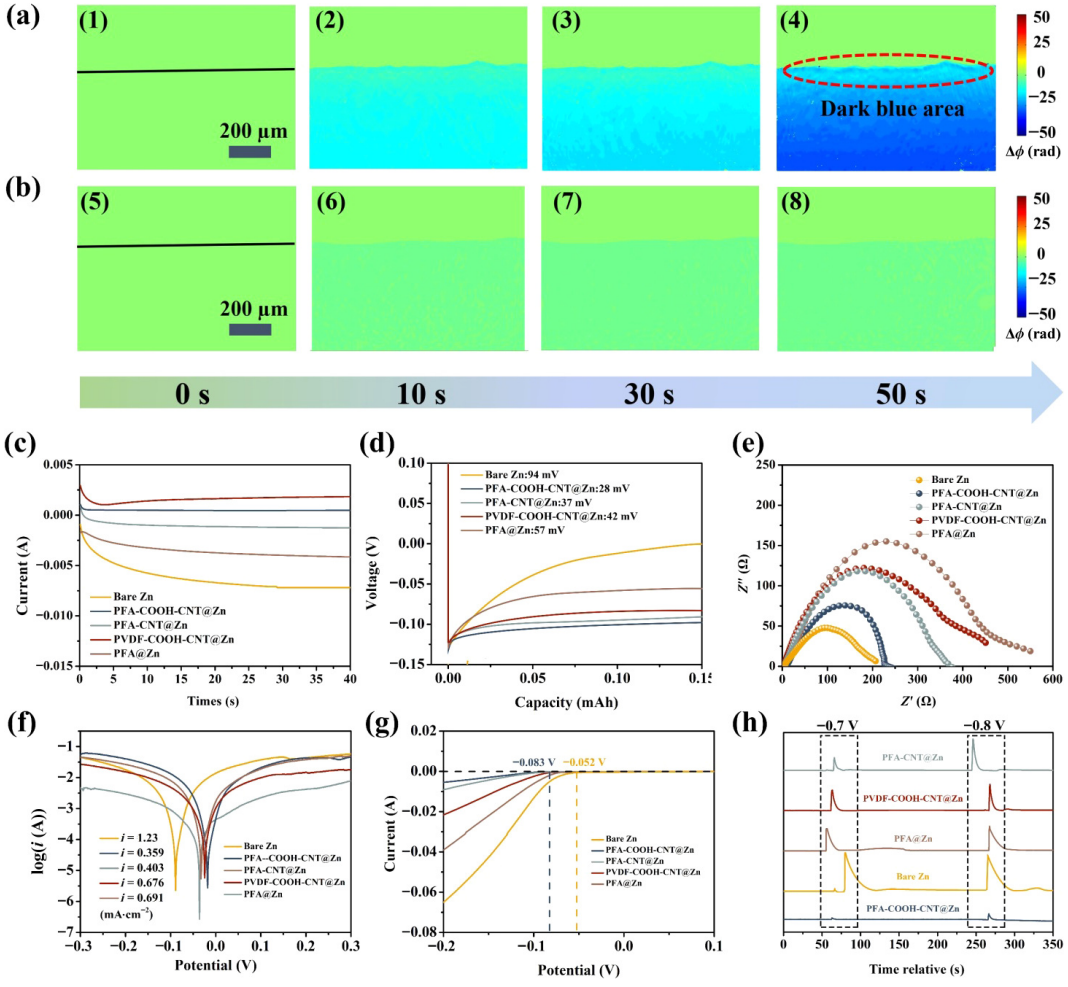

Figure 5 Electrochemical characterizations for explaining the mechanisms. (a) The phase map of the interface between naked Zn anode and electrolyte at different deposition times ((1): 0 s, (2): 10 s, (3): 30 s, (4): 50 s), (b) The phase map of the interface between naked PFA-COOH-CNT@Zn anode and electrolyte at different deposition times ((5): 0 s, (6): 10 s, (7): 30 s, (8): 50 s). (c) CA curves of the Zn||Ti half cells with using bare Zn, PFA@Zn, PFA@CNT@Zn, PVDF-COOH-CNT@Zn, and PFA-COOH-CNT@Zn anodes. (d) Nucleation overpotential curves of Zn||Zn symmetric cells using various Zn anodes. (e) EIS curve of the Zn||Zn symmetric cells. (f) Tafel curves of Zn||Zn symmetric cells using various Zn anodes. (g) LSV curves of the Zn||Zn symmetric cells. (h) DEMS curves of using various Zn anodes.

for Zn||Zn symmetric cell based on PFA-COOH-CNT@Zn anode quickly stabilizes within 10 s, quicker than that of other Zn||Zn symmetric cells using the naked Zn, PFA-CNT@Zn, PFA@Zn, and PVDF-COOH@Zn anodes. The current steadily increasing suggests that Zn^{2+} diffuses in two dimensions (2D) to form dendrites on the zinc anode surface, whereas the current rapidly stabilizing indicates that Zn^{2+} diffusion transitions from 2D to 3D, forcing zinc ions to closely nucleate and encouraging uniform growth [43]. The nucleation overpotential is very important for the dendrite formation and growth. When the nucleation overpotential is low, the nucleation and growth barrier of zinc metal is small, which contributes to the uniform nucleation of zinc on the electrode surface and reduces the formation of dendrites [44]. On the contrary, high nucleation overpotential may increase the risk of zinc dendrite formation [45]. As can be seen in Fig. 5(d), PFA-COOH-CNT@Zn anode exhibits the lowest nucleation overpotential compared to other Zn anodes, indicating the abundant oxygen-containing functional groups on PFA-COOH-CNT can provide more nucleation sites and promote small nuclear radius formation of Zn^{2+} and continuous three-dimensional diffusion [46]. The EIS curves of Zn||Zn symmetric batteries are shown in Fig. 5(e) ahead of cycling with various Zn anodes. As observed, the naked Zn anode shows the smallest charge transfer resistance, which is because zinc metal itself has good electrical conductivity. After constructing the polymer-based artificial SEI films on Zn anode surfaces, the charge transfer resistances have increased, particularly the PFA@Zn anode shows the highest charge transfer resistance, which is because of the high insulation of PFA. Therefore, the introduction of a conductive carbon matrix is indispensable. After introduction of the COOH-CNT, the charge transfer resistance of PFA-COOH-CNT@Zn almost not increase, which will also guarantee the construction of PFA-COOH-CNT artificial SEI film to lower Zn^{2+} diffusion energy and facilitate faster charge transfer and more efficient nucleation kinetics [47].

In order to further confirm the impact of PFA-COOH-CNT hydrophobicity on the anti-corrosion of zinc anodes, the *ex-situ* electrochemical characterizations, Tafel, LSV and DMES electrochemical characterizations were investigated. Among Tafel test was conducted on symmetric batteries with different SEI films coated anodes and bare zinc anodes to explore the enhancement of zinc foil corrosion resistance. As depicted in Fig. 5(f), the corrosion current density for PFA-COOH-CNT@Zn anode is the smallest,

lower than that of PFA@Zn, PVDF-COOH-CNT@Zn and PFA-CNT@Zn, and far lower than that of bare Zn anode, indicating its good corrosion resistance, which may be due to its good hydrophobicity and optimal zincophilic property, which can inhibit HER and other chemical corrosion at the same time, so that the corrosion current density is the lowest. Additionally, the corrosion potential of PFA-COOH-CNT@Zn is also significantly higher than that of bare Zn anode (−0.024 V vs. −0.089 V), also signifying a significant improvement in corrosion resistance with PFA-COOH-CNT SEI film. Consistent with Tafel results, LSV curves also demonstrate similar trends. As depicted in Fig. 5(g), PFA-COOH-CNT@Zn exhibits the lowest hydrogen evolution overpotential (−0.096 V), significantly lower than bare Zn (−0.052 V), indicating the good inhibition of HER by PFA-COOH-CNT@Zn. To further demonstrate this inhibition during zinc stripping/electroplating, *in-situ* DEMS was finally studied. As depicted in Fig. 5(h), using the naked Zn anode, the hydrogen production intensity is the biggest, following using the PFA-CNT@Zn, PVDF-COOH-CNT@Zn, and PFA@Zn anodes, and the hydrogen production intensity is lowest using the PFA-COOH-CNT@Zn anode, which this changing trend is consistent with the Tafel and LSV results, once again suggesting the effectiveness at inhibiting hydrogen evolution corrosion reaction with using these SEI films and the superiority of PFA-COOH-CNT SEI film [12]. Taken together with the aforementioned results, it is evident that PFA-COOH-CNT can physically isolate water from immediate contact with the Zn anode, thereby enhancing the corrosion resistance of the zinc anode and ensuring stability.

Finally, to verify the practicability of PFA-COOH-CNT@Zn anode, the electrochemical performances of the Zn-V_2O_5 full cells were examined. Figure S6 in the ESM shows the cyclic voltametric (CV) curves of all the Zn-V_2O_5 full cells for the first three cycles at 0.2 mV·s^{-1} (versus Zn^{2+}/Zn), and all electrodes show two pair redox peaks, corresponds to the reduction of V^{5+}/V^{4+} and V^{4+}/V^{3+}. Furthermore, the third cycle of the CV curves in Fig. 6(a) compares the differences among the samples. As illustrated, for bare Zn||V_2O_5 battery, it shows the most obvious polarization on redox peaks compared to the other full batteries. And the PFA-COOH-CNT@Zn||V_2O_5 exhibits the strongest peak intensity of V^{5+}/V^{4+} oxidation peak, which is possibly attributed to the fast deintercalation kinetics due to the large interlayer spacing [48].

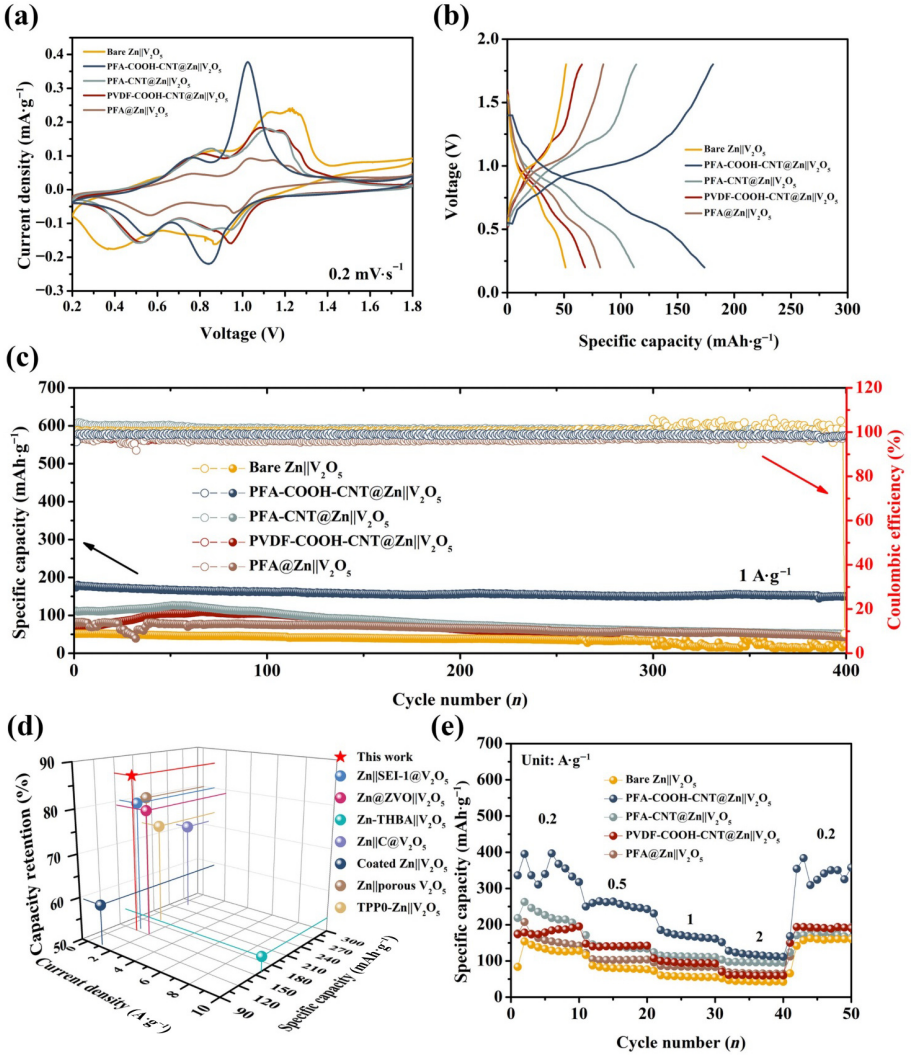

Figure 6 Electrochemical performances of Zn||V_2O_5 full cells. (a) The CV curves of PFA-COOH-CNT@Zn||V_2O_5 full cells, scan rate: 0.2 mV·s^{-1}. (b) Galvanostatic charge/discharge curves for various full cells at test current of 1 A·g^{-1}, (c) The long-cycling performance of V_2O_5-based full cells at 1 A·g^{-1}. (d) Full cells electrochemical performances comparison. (e) The rate performances of full cells at currents between 0.2 and 2 A·g^{-1}.

Additionally, the voltage gaps of the redox pairs in all full cells are shown in Fig. S6(f) in the ESM. The PFA-COOH-CNT@Zn||V_2O_5 reveals the smallest voltage gaps of both V^{5+}/V^{4+} and V^{4+}/V^{3+} redox pairs compared to the other full cells, suggesting the rapid ion diffusion and fast redox reaction kinetics [49]. And the galvanostatic discharge/charge curve in Fig. 6(b) shows all the full batteries exhibit two discharge plateaus at around 0.8 and 0.5 V, corresponding well with the reduction peaks in CV curves. And the PFA-COOH-CNT@Zn||V_2O_5 demonstrates longer charge/discharge voltage plateaus and a smaller gap in charge/discharge potential, also indicating the excellent reversible capability and weaker polarization of PFA-COOH-CNT@Zn||V_2O_5 full battery [12]. The cycling stability in Fig. 6(c) shows that the full cell with using the PFA-COOH-CNT@Zn anode demonstrates far higher cycling stability than that of utilizing bare Zn, PFA@Zn, PFA-CNT@Zn, and PVDF-COOH-CNT@Zn anodes, whose reversible capacity increases to 150.2 mAh·g^{-1} after 400 cycles with a capacity retention rate of 86.4%. The capacity retention and cycling stability for PFA-COOH-CNT@Zn||V_2O_5 full cell are even better than previous research (Fig. 6(d) and Table S3 in the ESM). Furthermore, the rate performances of the assembled full cells are displayed in Fig. 6(e). It is clear that full cells employing PFA-COOH-CNT@Zn anode outperform full cells using naked Zn anode or other SEI film coated Zn anodes. At a high rate of 2.0 A·g^{-1}, the discharge capacity of PFA-COOH-CNT@Zn||V_2O_5 full cell can reach as high as 124 mAh·g^{-1} and when the current switches from 2 to 0.2 A·g^{-1}, the full cell discharge capacity of COOH-CNT@Zn||V_2O_5 could return more closely to its starting value. The excellent electrochemical performances proves the significant contribution of the zincophilic and hydrophobic PFA-COOH-CNT SEI film in improving the utility of zinc anode.

4 Conclusions

A hydrophobic and zincophilic PFA-COOH-CNT SEI film has been successfully constructed on Zn anode by a simple *in-situ* reaction of FA with COOH-CNT. The abundant oxygen-containing groups in PFA-COOH-CNT SEI film could effectively induce the Zn^{2+} uniform deposition to realize the dendrite growth inhibition, and simultaneously the carbon skeleton and alkyl chain in PFA-COOH-CNT SEI film could isolate the H_2O directly attacking the Zn anode to realize the inhibition of HER and passivation. Finally, the Zn anode with such SEI film demonstrates excellent cycling stability that can cycle more than 2200 h at 1 mA·cm^{-2}, 1 mAh·cm^{-2}, and the corresponding PFA-COOH-CNT@Zn||V_2O_5 full cell also exhibits a high reversible capacity with high coulombic efficiency. In a word, this work offers an easy-to-implement method for the metal negative electrode employed in various energy storage systems.

Electronic Supplementary Material: Supplementary material is available in the online version of this article at https://doi.org/10.26599/NR.2025.94907156.

Data availability

All data needed to support the conclusions in the paper are presented in the manuscript and the Electronic Supplementary Material. Additional data related to this paper may be requested from the corresponding author upon request.

Acknowledgements

This study was funded by the National Natural Science Foundation of China (Nos. 51902036, 22222902, 2263203, and 52111530236), the National Key R&D Program of China (No. 2022YFA1203902), the Key Science and Technology Research Program of Chongqing Education Commission (No. KJZD-K202200807), the Natural Science Foundation of Chongqing Science & Technology Commission (No. CSTB2022NSCQ-MSX0828), Chongqing Bayu Scholars Support Program (No. YS2022050), and Research Project of Innovative Talent Training Engineering Program of Chongqing Primary and Secondary School (No. CY240806).

Declaration of competing interest

All the contributing authors report no conflict of interests in this work.

Author contribution statement

L. Y. K.: Data curation, experimental design, validation, writing original manuscript, experimental design. B. H. X.: Data curation, calculation, experimental design, writing original manuscript. L. Z.: Results analysis and manuscript discussions. Z. S. L.: Project administration and results discussions. X. X. G.: Project administration, funding acquisition, writing origianl manuscript and manuscript discussions. X. L. R.: Characterizations and manuscript discussions. Y. L. H.: Project administration, funding acquisition, revised manuscript. All the authors have approved the final manuscript.

Use of AI statement

None.

References

[1] Blanc, L. E.; Kundu, D.; Nazar, L. F. Scientific challenges for the implementation of Zn-ion batteries. *Joule* **2020**, *4*, 771–799.
[2] Li, G. J.; Lou, X. Y.; Peng, C. B.; Liu, C. T.; Chen, W. H. Interface chemistry for sodium metal anodes/batteries: A review. *Chem. Synth.* **2022**, *2*, 16.
[3] Service, R. F. Zinc aims to beat lithium batteries at storing energy. *Science,* **2021**, *372*, 890–891.
[4] Zhang, J. L.; Shi, M. Y.; Gao, H. W.; Ren, X. X.; Cao, J. C.; Li, G. J.; Wang, A. X.; Liu, C. T. Engineering interfaces of zinc metal anode for stable batteries. *Chem. Eng. J.* **2024**, *491*, 152050.
[5] Kundu, D.; Adams, B. D.; Duffort, V.; Vajargah, S. H.; Nazar, L. F. A high-capacity and long-life aqueous rechargeable zinc battery using a metal oxide intercalation cathode. *Nat. Energy* **2016**, *1*, 16119.
[6] Song, M.; Tan, H.; Chao, D. L.; Fan, H. J. Recent advances in Zn-ion batteries. *Adv. Funct. Mater.* **2018**, *28*, 1802564.
[7] Zhao, C. H.; Wang, X. L.; Shao, C. L.; Li, G. P.; Wang, J. X.; Liu, D. T.; Dong, X. T. The strategies of boosting the performance of highly reversible zinc anodes in zinc-ion batteries: Recent progress and future perspectives. *Sustain. Energy Fuels* **2021**, *5*, 332–350.
[8] Xu, C. J.; Li, B. H.; Du, H. D.; Kang, F. Y. Energetic zinc ion chemistry: The rechargeable zinc ion battery. *Angew. Chem., Int. Ed.* **2012**, *51*, 933–935.
[9] Zhang, M. H.; Su, Y.; Li, G. P.; Tang, B. Y.; Zhou, S.; Wang, X. L.; Liu, D. T.; Zhu, G. S. One-Pot preparation of microporous-polymer protected 3D porous Zn anode to enable advanced aqueous zinc batteries. *J. Power Sources* **2024**, *589*, 233755.

[10] Yin, Y. B.; Wang, S. N.; Zhang, Q.; Song, Y.; Chang, N. N.; Pan, Y. W.; Zhang, H. M.; Li, X. F. Dendrite-free zinc deposition induced by tin-modified multifunctional 3D host for stable zinc-based flow battery. *Adv. Mater.* **2020**, *32*, 1906803.
[11] Tao, F.; Feng, K. J.; Liu, Y.; Ren, J. Z.; Xiong, Y.; Li, C. B.; Ren, F. Z. Suppressing interfacial side reactions of zinc metal anode via isolation effect toward high-performance aqueous zinc-ion batteries. *Nano Res.* **2023**, *16*, 6789–6797.
[12] Gu, X. X.; Du, Y. X.; Ren, X. L.; Ma, F. C.; Zhang, X. F.; Li, M.; Wang, Q. H.; Zhang, L.; Lai, C.; Zhang, S. Q. Shielding-anchoring double protection tactics of imidazo[1,2-b]pyridazine additive for ultrastable zinc anode. *Adv. Funct. Mater.* **2024**, *34*, 2316541.
[13] Yang, X. Z.; Li, W. P.; Lv, J. Z.; Sun, G. J.; Shi, Z. X.; Su, Y. W.; Lian, X. Y.; Shao, Y. Y.; Zhi, A. M.; Tian, X. Z. et al. *In situ* separator modification via CVD-derived N-doped carbon for highly reversible Zn metal anodes. *Nano Res.* **2022**, *15*, 9785–9791.
[14] Ge, X. S.; Zhang, W. H.; Song, F. C.; Xie, B.; Li, J. D.; Wang, J. Z.; Wang, X. J.; Zhao, J. W.; Cui, G. L. Single-ion-functionalized nanocellulose membranes enable lean-electrolyte and deeply cycled aqueous zinc-metal batteries. *Adv. Funct. Mater.* **2022**, *32*, 2200429.
[15] Su, Y.; Wang, X. L.; Zhou, S.; Zou, X. Q.; Sun, H. Z.; Liu, D. T.; Zhu, G. S. A specific free-volume network as synergistic zinc-ion-conductor interface towards stable zinc anode. *Energy Storage Mater.* **2022**, *53*, 909–916.
[16] Liu, P. G.; Guo, J.; Chen, X. Y.; Wang, T.; Huang, Y. P.; Gao, S. S.; Wang, T.; Wu, D. L.; Liu, K. Y. A zincophilic molecular brush for a dendrite-free, corrosion-resistant, zinc metal anode with a long life cycle. *Nano Res.* **2024**, *17*, 390–396.
[17] Zhang, H.; Jiang, T. T.; Jin, D.; Xie, L. H.; Wu, M. Z. Hydrophobic and zincophilic organic hierarchical nano-membranes with ordered molecular packing for stable zinc metal anodes. *Energy Storage Mater.* **2024**, *70*, 103513.
[18] Zhou, X.; Chen, R. P.; Cui, E. H.; Liu, Q.; Zhang, H.; Deng, J. H.; Zhang, N. N.; Xie, C.; Xu, L.; Mai, L. A novel hydrophobic-zincophilic bifunctional layer for stable Zn metal anodes. *Energy Storage Mater.* **2023**, *55*, 538–545.
[19] Zhang, R. C.; Feng, Y.; Ni, Y. X.; Zhong, B. D.; Peng, M. Y.; Sun, T. J.; Chen, S.; Wang, H.; Tao, Z. L.; Zhang, K. Bifunctional interphase with target-distributed desolvation sites and directionally depositional ion flux for sustainable zinc anode. *Angew. Chem.* **2023**, *135*, e202304503.
[20] Di, S. L.; Nie, X. Y.; Ma, G. Q.; Yuan, W. T.; Wang, Y. Y.; Liu, Y. C.; Shen, S. G.; Zhang, N. Zinc anode stabilized by an organic–inorganic hybrid solid electrolyte interphase. *Energy Storage Mater.* **2021**, *43*, 375–382.
[21] Guo, S. J.; Yang, Q. S.; He, X. Q.; Liew, K. M. Design of 3D carbon nanotube-based nanostructures and prediction of their extra-strong mechanical properties under tension and compression. *Comp Mater. Sci.* **2014**, *85*, 324–331.
[22] Parker, J. F.; Nelson, E. S.; Wattendorf, M. D.; Chervin, C. N.; Long, J. W.; Rolison, D. R. Retaining the 3D framework of zinc sponge anodes upon deep discharge in Zn-air cells. *ACS Appl. Mater. Interfaces* **2014**, *6*, 19471–19476.
[23] Huang, J. Q.; Hou, Z.; Gao, P. S.; Yan, X. F.; Lin, X. Y.; Zhang, B. A freestanding hydroxylated carbon nanotube film boosting the stability of Zn metal anodes. *Mater. Today Commun.* **2022**, *32*, 103939.
[24] Feng, Y. G.; Wang, Y. D.; Sun, L.; Zhang, K. Q.; Liang, J. C.; Zhu, M. F.; Tie, Z.; Jin, Z. Fluorinated interface engineering toward controllable zinc deposition and rapid cation migration of aqueous Zn-Ion batteries. *Small* **2023**, *19*, 2302650.
[25] Liu, C. Z.; Xu, W. W.; Zhang, L.; Zhang, D. T.; Xu, W. N.; Liao, X. B.; Chen, W. M.; Cao, Y. Z.; Li, M. C.; Mei, C. T. et al. Electrochemical hydrophobic tri-layer interface rendered mechanically graded solid electrolyte interface for stable zinc metal anode. *Angew. Chem., Int. Ed.* **2024**, *63*, e202318063.
[26] Clark, S. J.; Segall, M. D.; Pickard, C. J.; Hasnip, P. J.; Probert, M. I. J.; Refson, K.; Payne, M. C. First principles methods using CASTEP. *Z. Kristallogr. Cryst. Mater.* **2005**, *220*, 567–570.
[27] Pfrommer, B. G.; Côté, M.; Louie, S. G.; Cohen, M. L. Relaxation of crystals with the quasi-newton method. *J. Comput. Phys.* **1997**, *131*, 233–240.
[28] Perdew, J. P.; Burke, K.; Ernzerhof, M. Generalized gradient approximation made simple. *Phys. Rev. Lett.* **1996**, *77*, 3865–3868.
[29] Hammer, B.; Hansen, L. B.; Nørskov, J. K. Improved adsorption energetics within density-functional theory using revised perdew-burke-ernzerhof functionals. *Phys. Rev. B* **1999**, *59*, 7413–7421.
[30] Monkhorst, H. J.; Pack, J. D. Special points for brillouin-zone integrations. *Phys. Rev. B* **1976**, *13*, 5188–5192.
[31] Cochet, M.; Maser, W. K.; Benito, A. M.; Callejas, M. A.; Martínez, M. T.; Benoit, J. M.; Schreiber, J.; Chauvet, O. Synthesis of a new polyaniline/nanotube composite: "*In-situ*" polymerisation and charge transfer through site-selective interaction. *Chem. Commun*. **2001**, 1450–1451.
[32] Yao, X.; Wu, H. X.; Wang, J.; Qu, S.; Chen, G. Carbon nanotube/poly(methyl methacrylate) (CNT/PMMA) composite electrode fabricated by *in situ* polymerization for microchip capillary electrophoresis. *Chem.—Eur. J.* **2007**, *13*, 846–853.
[33] Dante, R. C.; Santamaria, D. A.; Gil, J. M. Crosslinking and thermal stability of thermosets based on novolak and melamine. *J. Appl. Polym. Sci.* **2009**, *114*, 4059–4065.
[34] Noparvar-Qarebagh, A.; Roghani-Mamaqani, H.; Salami-Kalajahi, M. Functionalization of carbon nanotubes by furfuryl alcohol moieties for preparation of novolac phenolic resin composites with high carbon yield values. *Colloid Polym. Sci.* **2015**, *293*, 3623–3631.
[35] Wu, S. X.; Yang, Y. J.; Liu, C. B.; Liu, T. F.; Zhang, Y. P.; Zhang, B. K.; Luo, D.; Pan, F.; Lin, Z. *In-situ* polymerized binder: A three-in-one design strategy for all-integrated SiO_x anode with high mass loading in lithium ion batteries. *ACS Energy Lett.* **2021**, *6*, 290–297.
[36] Guigo, N.; Mija, A.; Vincent, L.; Sbirrazzuoli, N. Chemorheological analysis and model-free kinetics of acid catalysed furfuryl alcohol polymerization. *Phys. Chem. Chem. Phys.* **2007**, *9*, 5359–5366.
[37] Shi, M. Y.; Zhang, J. L.; Tang, G. C.; Wang, B.; Wang, S.; Ren, X. X.; Li, G. J.; Chen, W. H.; Liu, C. T.; Shen, C. Y. Polyzwitterionic cross-linked double network hydrogel electrolyte enabling high-stable Zn anode. *Nano Res.* **2024**, *17*, 5278–5287.
[38] Wu, D. X.; Wang, C. Y.; Wu, M. G.; Chao, Y. F.; He, P. B.; Ma, J. M. Porous bowl-shaped VS_2 nanosheets/graphene composite for high-rate lithium-ion storage. *J. Energy Chem.* **2020**, *43*, 24–32.
[39] Siddique, A. B.; Pramanick, A. K.; Chatterjee, S.; Ray, M. Amorphous carbon dots and their remarkable ability to detect 2,4,6-trinitrophenol. *Sci. Rep.* **2018**, *8*, 9770.
[40] Xiao, J.; Li, Q. Y.; Bi, Y. J.; Cai, M.; Dunn, B.; Glossmann, T.; Liu, J.; Osaka, T.; Sugiura, R.; Wu, B. B. et al. Understanding and applying coulombic efficiency in lithium metal batteries. *Nat. Energy* **2020**, *5*, 561–568.
[41] Li, G. P.; Wang, Y.; Su, Y.; Fu, X. Q.; Wang, X. L.; Wang, J. X.; Lv, S. H.; Yu, W. S.; Dong, X. T.; Liu, D. T. A porous polycaprolactone coating with abundant ester groups for stable Zn metal anodes. *J. Energy Storage* **2024**, *97*, 112790.
[42] Liu, X.; Han, Q. G.; Ma, Q. X.; Wang, Y. H.; Liu, C. G. Cellulose-acetate coating by integrating ester group with zinc salt for dendrite-free Zn metal anodes. *Small* **2022**, *18*, 2203327.
[43] Shi, Z. H.; Yang, M.; Ren, Y. F.; Wang, Y. Z.; Guo, J. H.; Yin, J.; Lai, F. L.; Zhang, W. L.; Chen, S. L.; Alshareef, H. N. et al. Highly reversible Zn anodes achieved by enhancing ion-transport kinetics and modulating Zn (002) deposition. *ACS Nano* **2023**, *17*, 21893–21904.

[44] Hu, L. T.; Xiao, P.; Xue, L. L.; Li, H. Q.; Zhai, T. Y. The rising zinc anodes for high-energy aqueous batteries. *EnergyChem* **2021**, *3*, 100052.

[45] Liang, P. C.; Yi, J.; Liu, X. Y.; Wu, K.; Wang, Z.; Cui, J.; Liu, Y. Y.; Wang, Y. G.; Xia, Y. Y.; Zhang, J. J. Highly reversible Zn anode enabled by controllable formation of nucleation sites for Zn-based batteries. *Adv. Funct. Mater.* **2020**, *30*, 1908528.

[46] Zhang, Q.; Luan, J. Y.; Tang, Y. G.; Ji, X. B.; Wang, H. Y. Interfacial design of dendrite-free zinc anodes for aqueous zinc-ion batteries. *Angew. Chem., Int. Ed.* **2020**, *59*, 13180–13191.

[47] Wang, X. Z.; Ding, G.; Ma, Z. P.; Xu, Z. M.; Feng, Y. B.; Gong, W. B.; Liu, C. L.; Tian, K. H.; Yong, Z. Z.; Li, Q. L. Synchronously nucleated inducing deposition of Zn^{2+} and homogenized electric field endowed by 3D porous host for dendrite-free Zn metal anodes. *Chem. Eng. J.* **2023**, *472*, 144996.

[48] Zong, Q.; Zhuang, Y. L.; Liu, C. F.; Kang, Q. L.; Wu, Y. Z.; Zhang, J. J.; Wang, J. Y.; Tao, D. W.; Zhang, Q. L.; Cao, G. Z. Dual effects of metal and organic ions Co-intercalation boosting the kinetics and stability of hydrated vanadate cathodes for aqueous zinc-ion batteries. *Adv. Energy Mater.* **2023**, *13*, 2301480.

[49] Jiang, H. M.; Zhang, Y. F.; Waqar, M.; Yang, J.; Liu, Y. Y.; Sun, J. J.; Feng, Z. Y.; Sun, J. G.; Pan, Z. H.; Meng, C. G. et al. Anomalous Zn^{2+} storage behavior in dual-ion-in-sequence reconstructed vanadium oxides. *Adv. Funct. Mater.* **2023**, *33*, 2213127.